SCATTERING AND THERMAL EMISSION FROM A TWO DIMENSIONAL PERIODIC SURFACE

J. T. Johnson, R. T. Shin and J. A. Kong

1. Introduction

Scattering from a one dimensional periodic surface has been studied extensively with a large number of techniques, including both approximate [1–3], and numerically exact [4–11] methods. Models for one dimensional periodic surface scattering have found application in a wide range of areas, ranging from optical grating design [8] to the prediction of wave propagation over the ocean [10]. In a more recent application, theories and experiments involving passive remote sensing of one dimensional periodic surfaces [11–16] have conclusively demonstrated the existence of a third Stokes parameter component of the thermal emission, U_B. Assumed to be non-zero only in polarimetric passive remote sensing, U_B is known to respond to the azimuthal anisotropy of the medium under view [17] and thus is currently being investigated for application to remote sensing of wind direction over the ocean [18–21].

The one dimensional periodic surface studies previously performed allow surfaces to be rough in one spatial direction only. Surface

profiles do not vary perpendicular to this direction, so that a "row" type structure results as shown in Figure 1. While there are many interesting surfaces which do have a row structure, more general surfaces vary in two spatial directions as shown in Figure 2 and therefore render the one dimensional models invalid. Scattering from two dimensional periodic surfaces has previously been studied in reference [22], in which a volume equivalent current moment method was applied to investigate the reflection characteristics of microwave absorbing materials. However, to date no numerically exact results for two dimensional surface polarimetric thermal emission have been presented, so that the extension of U_B properties observed in the one dimensional case to the two dimensional case remains uncertain. For example, a one dimensional periodic surface model allows no insight into the effect of varying levels of surface azimuthal anisotropy on U_B signatures since a one dimensionally rough surface represents only a limiting case of anisotropy.
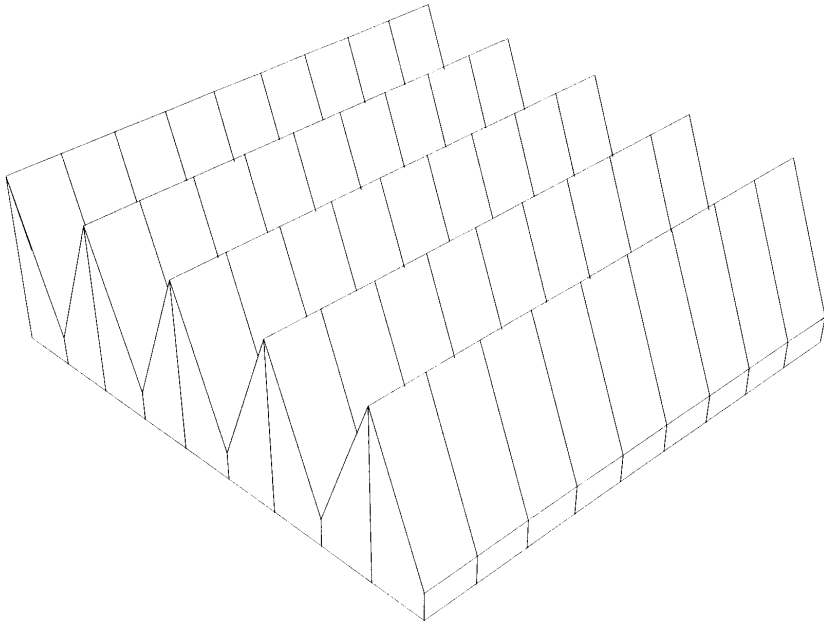

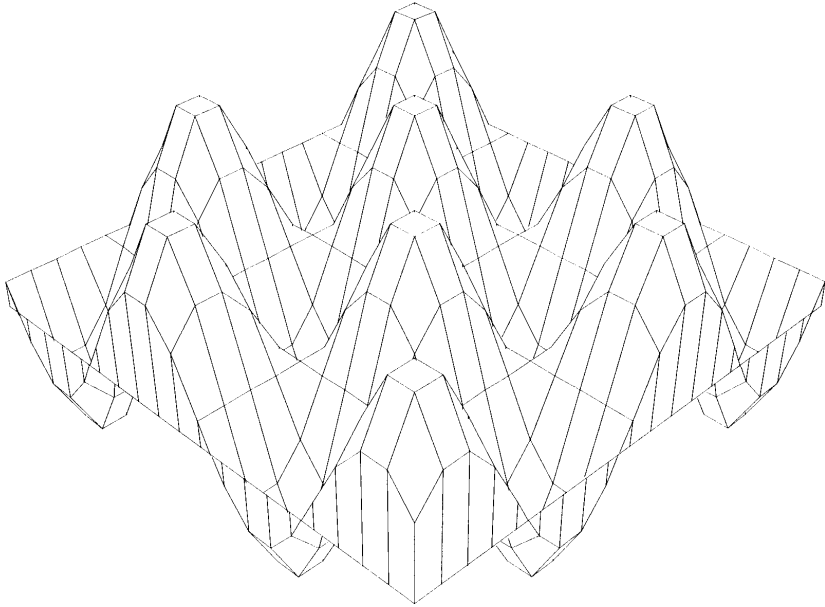Figure 1. Geometry of a one dimensional periodic surface.

Figure 2. Geometry of a two dimensional periodic surface.

In this paper, a numerically exact model for scattering from a two dimensional dielectric periodic surface is presented, based upon an extension of the extended boundary condition (EBC) technique for one dimensional periodic surfaces [7] to the two dimensional case. Since the region below the surface profile is considered to be a half space in this paper, use of a surface integral equation technique as opposed to the volume integral equations of [22] results in a more efficient solution. Although the limitations of the EBC method for surfaces with deep corrugations are well known [23], previous one dimensional periodic surface studies showed the EBC to perform efficiently for non-steep surfaces when compared to a method of moments approach [16]. Use of the EBC method for two dimensional surface profiles is motivated by the fact that computational requirements are much greater than in the one dimensional case, so that efficiency becomes an even more important issue if a thorough study is to be performed. Since properties of U_B for two dimensional surfaces can be studied within the limitations of the EBC, the method is adequate for the goals of this paper. Computational efficiency is further improved by performing required

integrals analytically over an arbitrary faceted surface profile.

The model is applied in a study of the response of U_B to the level of anisotropy of the medium under view. Calculations are performed for simple pyramidal surfaces, which reduce computational complexity and provide physical insight into the mechanisms which generate third Stokes parameter emission. Sensitivities of U_B to observation angle, pyramidal surface heights and lengths, and surface dielectric constants are studied, and illustrate that properties of U_B observed for one dimensional periodic surfaces remain similar in the two dimensional case.

The formulation of the extended boundary condition method is detailed in the next section, followed by a discussion of required integral evaluation in Section 3. The model is validated in Section 4 through reduction to the one dimensional periodic surface case, and convergence of predicted brightnesses with the number of surface field unknowns is discussed for two dimensional surfaces. A study of pyramidal surface polarimetric thermal emission in Section 5 is followed by conclusions in Section 6.

2. Formulation and Numerical Method

The extended boundary condition technique for periodic surface scattering involves solution of the Huygens' principle integral equations for unknown tangential electric and magnetic fields on a surface separating two homogeneous dielectric regions of space, labeled regions 0 and 1. The standard electric field integral equation (EFIE) [24] can be written as

$$\int_{-\infty}^{\infty} dS' \left\{ i\omega\mu \left(\overline{\overline{I}} + \frac{\nabla\nabla}{k_0^2} \right) g_0(\overline{r}, \overline{r}')[\hat{n}' \times \overline{H}(\overline{r}')] + \right.$$

$$\left. + \nabla g_0(\overline{r}, \overline{r}') \times [\hat{n}' \times \overline{E}(\overline{r}')] \right\} + \overline{E}_{inc}(\overline{r}) = \begin{cases} \overline{E}_0(\overline{r}) & z > z_s(x, y) \\ 0 & z < z_s(x, y) \end{cases} \quad (1)$$

where $\overline{E}_{inc}$ represents the incident electric field, taken to be a single incident plane wave with propagation vector $\overline{k}_i = \hat{x}k_{xi} + \hat{y}k_{yi} + \hat{z}k_{zi}$ in the following discussions, and $z_s(x, y)$ is a function describing the surface profile separating regions 0 and 1. It is assumed that the observation point $\overline{r}$ does not coincide with any of the source points $\overline{r}'$ in the integral equation, so that no singularities are encountered. The

scalar Green's function in the above equation is

$$g_j(\bar{r}, \bar{r}') = \frac{e^{ik_j|\bar{r}-\bar{r}'|}}{4\pi|\bar{r}-\bar{r}'|} \tag{2}$$

where k_j represents the electromagnetic wave number in regions $j = 0$ or $j = 1$ respectively. A similar integral equation can be written for the electric field in the region below the surface,

$$-\int_{-\infty}^{\infty} dS' \left\{ i\omega\mu \left(\overline{\overline{I}} + \frac{\nabla\nabla}{k_1^2} \right) g_1(\bar{r}, \bar{r}')[\hat{n}' \times \overline{H}(\bar{r}')] + \right.$$
$$\left. + \nabla g_1(\bar{r}, \bar{r}') \times [\hat{n}' \times \overline{E}(\bar{r}')] \right\} = \begin{cases} \overline{E}_1(\bar{r}) & z < z_s(x, y) \\ 0 & z > z_s(x, y) \end{cases} \tag{3}$$

If the surface height function is assumed to be periodic in both the x and y directions, so that $z_s(x + P_x, y) = z_s(x, y)$ and $z_s(x, y + P_y) = z_s(x, y)$, integration regions in the above integral equations can be reduced to a single period through the use of a periodic Green's function. Such Green's functions are well known and have been derived elsewhere [24] as

$$g_{Pj} = \frac{i}{P_x P_y} \sum_{m=-\infty}^{\infty} \sum_{n=-\infty}^{\infty} \frac{1}{2k_{zj_{mn}}} e^{i[k_{xn}(x-x')+k_{ym}(y-y')+k_{zj_{mn}}|z-z'|]} \tag{4}$$

where the spectral form of the periodic Green's function has been used, $k_{xn} = k_{xi} + \frac{2\pi n}{P_x}$, $k_{ym} = k_{yi} + \frac{2\pi m}{P_y}$ and $k_{zj_{mn}} = \sqrt{k_j^2 - k_{xn}^2 - k_{ym}^2}$. The branch cut of the square root function for $k_{zj_{mn}}$ is defined so that $\sqrt{-1} = +i$. Upon substitution of this Green's function into the integral equations, and assuming observation points above or below the points of maximum and minimum surface height respectively, integral equations (1) and (3) become

$$\overline{E}_{inc}(\bar{r}) + \sum_{m=-\infty}^{\infty} \sum_{n=-\infty}^{\infty} \bar{a}_{mn} e^{i\bar{k}_{mn0}^+\cdot\bar{r}} = \overline{E}_0(\bar{r}) \quad z > z_s(x, y)_{max} \tag{5}$$

$$\overline{E}_{inc}(\bar{r}) + \sum_{m=-\infty}^{\infty} \sum_{n=-\infty}^{\infty} \bar{b}_{mn} e^{i\bar{k}_{mn0}^-\cdot\bar{r}} = 0 \quad\quad z < z_s(x, y)_{min} \tag{6}$$

$$\sum_{m=-\infty}^{\infty} \sum_{n=-\infty}^{\infty} \overline{c}_{mn} e^{i\overline{k}_{mn1}^{-}\cdot\overline{r}} = -\overline{E}_1(\overline{r}) \qquad z < z_s(x,y)_{min} \qquad (7)$$

$$\sum_{m=-\infty}^{\infty} \sum_{n=-\infty}^{\infty} \overline{d}_{mn} e^{i\overline{k}_{mn1}^{+}\cdot\overline{r}} = 0 \qquad z > z_s(x,y)_{max} \qquad (8)$$

where

$$\bar{a}_{mn} = \frac{i}{2P_x P_y k_{z0_{mn}}} \int_P dS' e^{-i\overline{k}_{mn0}^{+}\cdot\overline{r}} \left\{ i\omega\mu \left(\overline{\overline{I}} - \hat{k}_{mn0}^{+}\hat{k}_{mn0}^{+}\right)[\hat{n}' \times \overline{H}(\overline{r}')] + \right.$$
$$\left. +i\overline{k}_{mn0}^{+} \times [\hat{n}' \times \overline{E}(\overline{r}')] \right\} \qquad (9)$$

$$\bar{b}_{mn} = \frac{i}{2P_x P_y k_{z0_{mn}}} \int_P dS' e^{-i\overline{k}_{mn0}^{-}\cdot\overline{r}} \left\{ i\omega\mu \left(\overline{\overline{I}} - \hat{k}_{mn0}^{-}\hat{k}_{mn0}^{-}\right)[\hat{n}' \times \overline{H}(\overline{r}')] + \right.$$
$$\left. +i\overline{k}_{mn0}^{-} \times [\hat{n}' \times \overline{E}(\overline{r}')] \right\} \qquad (10)$$

$$\bar{c}_{mn} = \frac{i}{2P_x P_y k_{z1_{mn}}} \int_P dS' e^{-i\overline{k}_{mn1}^{-}\cdot\overline{r}} \left\{ i\omega\mu \left(\overline{\overline{I}} - \hat{k}_{mn1}^{-}\hat{k}_{mn1}^{-}\right)[\hat{n}' \times \overline{H}(\overline{r}')] + \right.$$
$$\left. +i\overline{k}_{mn1}^{-} \times [\hat{n}' \times \overline{E}(\overline{r}')] \right\} \qquad (11)$$

$$\bar{d}_{mn} = \frac{i}{2P_x P_y k_{z1_{mn}}} \int_P dS' e^{-i\overline{k}_{mn1}^{+}\cdot\overline{r}} \left\{ i\omega\mu \left(\overline{\overline{I}} - \hat{k}_{mn1}^{+}\hat{k}_{mn1}^{+}\right)[\hat{n}' \times \overline{H}(\overline{r}')] + \right.$$
$$\left. +i\overline{k}_{mn1}^{+} \times [\hat{n}' \times \overline{E}(\overline{r}')] \right\} \qquad (12)$$

and

$$\overline{k}_{mnj}^{\pm} = \hat{x}k_{xn} + \hat{y}k_{ym} \pm \hat{z}k_{zj_{mn}}$$

From equations (5) and (7), it is clear that the scattered field in region zero above the surface profile and the transmitted field in region one below the surface profile consist of a sum of upgoing and downgoing plane wave fields respectively, known as Floquet modes, with unknown vector amplitudes $\overline{a}_{mn}$ and $\overline{c}_{mn}$. These unknown amplitudes can be determined from equations (9) and (11) once tangential electric and magnetic fields at the surface boundary are known.

The formulation of equations (1) to (12) is general for two dimensional periodic surfaces. The EBC approach is based upon solution of vector equations (6) and (8) for the unknown tangential electric and magnetic fields, which involve the regions of "no-interest" in the Huygens' formulation. Use of these equations is advantageous because a knowledge of both tangential fields on the surface profile and the total

fields above or below the surface profile $\overline{E}_0$ and $\overline{E}_1$ is not required as in equations (5) and (7), and a simple mode matching technique can be applied to their solution. However, the non-local nature of equations (5) to (8) cause the previously mentioned conditioning problems for steep surfaces, as evanescent waves generated within the surface profile are modeled only after having been exponentially attenuated.

Applying the orthogonality property for plane wave fields in equations (6) and (8) yields the following vector equations

$$\overline{b}_{mn} = -\,\hat{e}_i\delta_{mn0} \tag{13}$$

$$\overline{d}_{mn} = 0 \tag{14}$$

where δ_{mn0} is one for $m = n = 0$ and zero otherwise and a plane wave incident field of $\overline{E}_{inc} = \hat{e}_i e^{i\overline{k}_i \cdot \overline{r}}$ has been assumed. Next, unknown tangential fields on the surface profile are written as

$$\hat{n}' \times \overline{H} = \hat{x}J_x + \hat{y}J_y + \hat{z}\left(\frac{\partial z_s}{\partial x'}J_x + \frac{\partial z_s}{\partial y'}J_y\right)$$

$$-\hat{n}' \times \overline{E} = \hat{x}M_x + \hat{y}M_y + \hat{z}\left(\frac{\partial z_s}{\partial x'}M_x + \frac{\partial z_s}{\partial y'}M_y\right)$$

where

$$\hat{n}' = \left\{\hat{z} - \frac{\partial z_s}{\partial x'}\hat{x} - \frac{\partial z_s}{\partial y'}\hat{y}\right\} \Big/ \sqrt{1 + \left(\frac{\partial z_s}{\partial x'}\right)^2 + \left(\frac{\partial z_s}{\partial y'}\right)^2}$$

and unknown surface field amplitudes are expanded in Fourier series as

$$J_x = \sum_o \sum_p q_{op} e^{ik_{xo}x' + ik_{yp}y'} \tag{15}$$

$$J_y = \sum_o \sum_p r_{op} e^{ik_{xo}x' + ik_{yp}y'} \tag{16}$$

$$M_x = -\sum_o \sum_p s_{op} e^{ik_{xo}x' + ik_{yp}y'} \tag{17}$$

$$M_y = -\sum_o \sum_p t_{op} e^{ik_{xo}x' + ik_{yp}y'} \tag{18}$$

Vector equations (13) and (14) each consist of one set of m times n equations for three Cartesian components. However, these six sets

of equations are restricted to four by the divergenceless condition of plane wave fields. Using the x and y components of these equations and substituting in the Fourier series expansions (15–18) results in the following matrix equation:

$$
\begin{bmatrix}
\overline{\overline{A}}_{xx0}^{-} & \overline{\overline{A}}_{xy0}^{-} & \overline{\overline{B}}_{xx0}^{-} & \overline{\overline{B}}_{xy0}^{-} \\
\overline{\overline{A}}_{yx0}^{-} & \overline{\overline{A}}_{yy0}^{-} & \overline{\overline{B}}_{yx0}^{-} & \overline{\overline{B}}_{yy0}^{-} \\
\overline{\overline{A}}_{xx1}^{+} & \overline{\overline{A}}_{xy1}^{+} & \overline{\overline{B}}_{xx1}^{+} & \overline{\overline{B}}_{xy1}^{+} \\
\overline{\overline{A}}_{yx1}^{+} & \overline{\overline{A}}_{yy1}^{+} & \overline{\overline{B}}_{yx1}^{+} & \overline{\overline{B}}_{yy1}^{+}
\end{bmatrix}
\begin{bmatrix}
q_{[op]} \\ r_{[op]} \\ s_{[op]} \\ t_{[op]}
\end{bmatrix}
=
\begin{bmatrix}
E_{x[mn]} \\ E_{y[mn]} \\ 0 \\ 0
\end{bmatrix}
\tag{19}
$$

where

$$
\left[\overline{\overline{A}}_{\alpha\beta j}^{\pm} \right]_{[mn][op]} =
$$
$$
\int_P dx' dy' \left\{ \frac{-\omega\mu}{2P_x P_y k_{z j_{mn}}} e^{-i(k_{xn}-k_{xo})x' - i(k_{ym}-k_{yp})y' - i(\pm k_{z j_{mn}})z'} \right.
$$
$$
\left. \sqrt{1 + \left(\frac{\partial z_s}{\partial x'}\right)^2 + \left(\frac{\partial z_s}{\partial y'}\right)^2} \, \hat{\alpha} \cdot \left(\overline{\overline{I}} - \hat{k}_{mnj}^{\pm} \hat{k}_{mnj}^{\pm} \right) \cdot \left(\hat{\beta} + \hat{z}\frac{\partial z_s}{\partial \beta} \right) \right\}
\tag{20}
$$

$$
\left[\overline{\overline{B}}_{\alpha\beta j}^{\pm} \right]_{[mn][op]} =
$$
$$
\int_P dx' dy' \left\{ \frac{i}{2P_x P_y k_{z j_{mn}}} e^{-i(k_{xn}-k_{xo})x' - i(k_{ym}-k_{yp})y' - i(\pm k_{z j_{mn}})z'} \right.
$$
$$
\left. \sqrt{1 + \left(\frac{\partial z_s}{\partial x'}\right)^2 + \left(\frac{\partial z_s}{\partial y'}\right)^2} \, i\hat{\alpha} \cdot \left[\overline{k}_{mnj}^{\pm} \times \left(\hat{\beta} + \hat{z}\frac{\partial z_s}{\partial \beta} \right) \right] \right\}
\tag{21}
$$

and

$$
E_{\alpha[mn]} = -\hat{\alpha} \cdot \hat{e}_i \delta_{mn0}
\tag{22}
$$

In the above notation, $[mn]$ references the row number of the matrix, while $[op]$ references the column. These indices actually are a single number, which is obtained by consecutively labeling the set of m times n scattered modes in two dimensions and the set of o times p Fourier series coefficients. The above matrix equation is infinitely large in theory, but must be truncated in order to be inverted. Convergence of model predictions with the number of equations retained will be discussed in Section 4. Matrix elements can be calculated once the surface

profile is specified, and the matrix can be inverted to obtain Fourier series expansion coefficients of unknown surface fields, $q_{op}, r_{op}, s_{op},$ and t_{op}. These expansion coefficients can then be substituted into equations (9) and (11), which involve integrals similar to the matrices $\overline{\overline{A}}$ and $\overline{\overline{B}}$ above, to determine vector amplitudes of the reflected and transmitted Floquet modes, $\overline{a}_{[mn]}$ and $\overline{c}_{[mn]}$ respectively, as

$$
\begin{bmatrix}
\overline{\overline{A}}_{xx0}^{+} & \overline{\overline{A}}_{xy0}^{+} & \overline{\overline{B}}_{xx0}^{+} & \overline{\overline{B}}_{xy0}^{+} \\
\overline{\overline{A}}_{yx0}^{+} & \overline{\overline{A}}_{yy0}^{+} & \overline{\overline{B}}_{yx0}^{+} & \overline{\overline{B}}_{yy0}^{+} \\
\overline{\overline{A}}_{xx1}^{-} & \overline{\overline{A}}_{xy1}^{-} & \overline{\overline{B}}_{xx1}^{-} & \overline{\overline{B}}_{xy1}^{-} \\
\overline{\overline{A}}_{yx1}^{-} & \overline{\overline{A}}_{yy1}^{-} & \overline{\overline{B}}_{yx1}^{-} & \overline{\overline{B}}_{yy1}^{-}
\end{bmatrix}
\begin{bmatrix}
q_{[op]} \\
r_{[op]} \\
s_{[op]} \\
t_{[op]}
\end{bmatrix}
=
\begin{bmatrix}
a_{x[mn]} \\
a_{y[mn]} \\
c_{x[mn]} \\
c_{y[mn]}
\end{bmatrix}
\tag{23}
$$

Components of $\overline{a}_{[mn]}$ and $\overline{c}_{[mn]}$ in the $\hat{z}$ direction are obtained from the divergence condition as

$$
a_{z[mn]} = -\frac{1}{k_{z0_{mn}}}\left(k_{xn}a_{x[mn]} + k_{ym}a_{y[mn]}\right)
$$

$$
c_{z[mn]} = \frac{1}{k_{z1_{mn}}}\left(k_{xn}c_{x[mn]} + k_{ym}c_{y[mn]}\right)
$$

3. Evaluation of Required Integrals

Construction of matrix equation (19) requires evaluation of the integrals of (20) and (21) for each combination of $[mn]$ and $[op]$ indices. There are many options for evaluating these integrals, ranging from a fully numerical integration scheme to an FFT based method in which the $e^{-i(\pm k_{zjmn})z'}$ term inside the integral is expanded in a Fourier series. In this paper, a method in which the surface profile is assumed to be made up of triangular facets is adopted, and resulting integrals over individual surface facets are performed analytically. This approach should be an efficient technique for surfaces that are accurately described in terms of a small number of triangular facets, such as the pyramidal type surface illustrated in Figure 3.
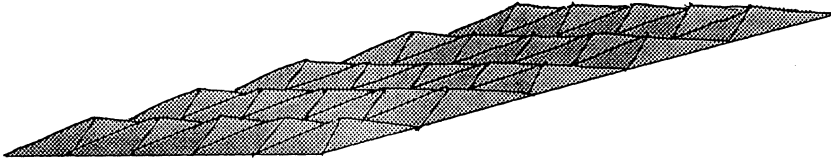
Figure 3. Geometry of a two dimensional pyramidal surface.

Consider a triangular grid in the $x - y$ plane, shown in Figure 4, for which surface heights above the $x - y$ plane are specified at each of the points $x_\gamma = (\gamma - 1)\Delta x$, $y_\delta = (\delta - 1)\Delta y$ on the grid, with $\gamma = 1, 3/2, 2, ...$ and $\delta = 1, 2, 3, ...$. A 4×8 point grid is assumed in Figure 4, with the lines $x = x_5$ and $y = y_9$ equivalent to $x = x_1$ and $y = y_1$ respectively due to surface periodicities. The particular structure of the grid in Figure 4 is chosen to enable simple construction of pyramidal type surfaces, as will be discussed in Section 5.
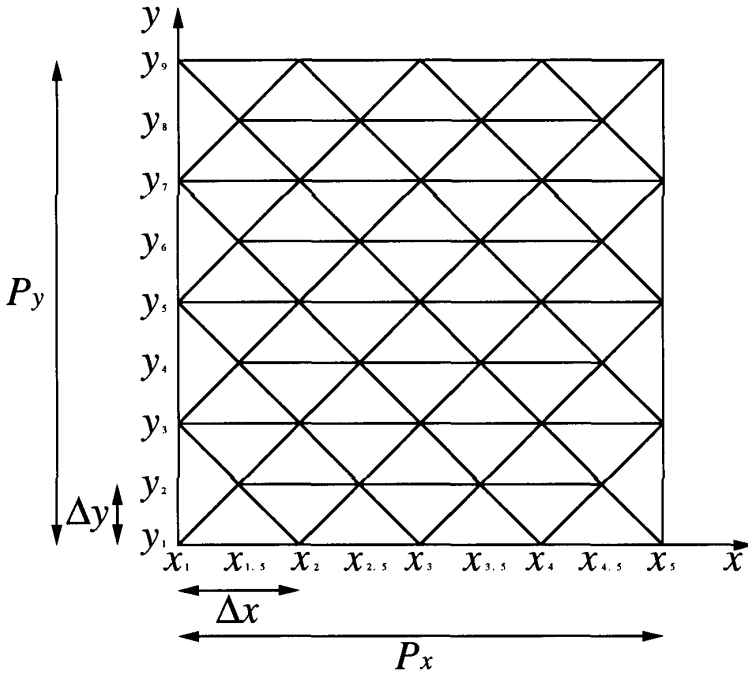

Figure 4. Triangular grid in $x - y$ plane for surface specification.

Since the integrals of (20) and (21) are over one period of the surface profile, matrix elements can be rewritten as a sum of the integrals over each individual triangular facet making up the profile. In addition, surface derivatives, $\frac{\partial z_s}{\partial x'}$ and $\frac{\partial z_s}{\partial y'}$ remain constant on an individual planar surface facet, so that vector product terms can be factored out of facet integrals. The resulting matrix elements are

$$\left[\overline{\overline{A}}^\pm_{\alpha\beta j} \right]_{[mn][op]} =$$

$$\frac{-\omega\mu}{2P_x P_y k_{zj_{mn}}} \sum_f \left\{ \sqrt{1 + \left(\frac{\partial z_s}{\partial x'}\right)^2 + \left(\frac{\partial z_s}{\partial y'}\right)^2} \left[\hat{\alpha} \cdot \left(\overline{\overline{I}} - \hat{k}^\pm_{mnj}\hat{k}^\pm_{mnj} \right) \cdot \right. \right.$$

$$\left. \left. \cdot \left(\hat{\beta} + \hat{z}\frac{\partial z_s}{\partial\beta} \right) \right] \int\!\!\int_{F_f} dx'dy' e^{-i(k_{xn}-k_{xo})x' - i(k_{ym}-k_{yp})y' - i(\pm k_{zj_{mn}})z'} \right\} \quad (24)$$

$$\left[\overline{\overline{B}}^\pm_{\alpha\beta j} \right]_{[mn][op]} =$$

$$\frac{i}{2P_x P_y k_{zj_{mn}}} \sum_f \left\{ \sqrt{1 + \left(\frac{\partial z_s}{\partial x'}\right)^2 + \left(\frac{\partial z_s}{\partial y'}\right)^2} i\hat{\alpha} \cdot \left[\overline{k}^\pm_{mnj} \times \left(\hat{\beta} + \hat{z}\frac{\partial z_s}{\partial\beta} \right) \right] \right.$$

$$\left. \int_{F_f} dx'dy' e^{-i(k_{xn}-k_{xo})x' - i(k_{ym}-k_{yp})y' - i(\pm k_{zj_{mn}})z'} \right\} \quad (25)$$

where F_f indicates the particular facet over which the integral is to be performed. From the above equations, it is clear that evaluation of the sixteen matrix elements for each $[mn]$ and $[op]$ combination actually requires calculation of only two integrals for each surface facet.

The surface profile of each triangular facet is simply a plane passing through the three points bounding the triangle. The equation of this plane is

$$z' = ax' + by' + c \quad (26)$$

where

$$a = \frac{z_2 - z_1}{\Delta x}$$

$$b = \frac{z_3 - (z_2 + z_1)/2}{\Delta y}$$

$$c = z_1 - ax_\gamma - by_\delta$$

and z_1, z_2, z_3, x_γ, and y_δ are as defined in Figure 5.

$$\left(x_{\gamma+0.5}, y_{\delta+1}, z_3\right)$$

$$\left(x_\gamma, y_\delta, z_1\right) \qquad \left(x_{\gamma+1}, y_\delta, z_2\right)$$
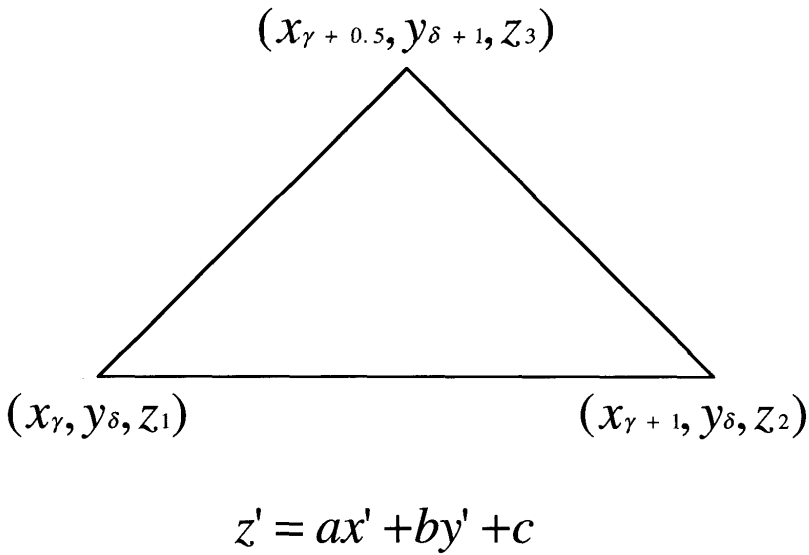
$$z' = ax' + by' + c$$

Figure 5. Definition of surface plane through triangle.

Upon substitution of this equation for z' into (24) and (25), integrals over each surface facet can be performed analytically. The necessary integrals are

$$I_{\gamma\delta}^{\pm} = e^{-i(\pm k_{zjmn}c)} \int_{F_f} dx'dy' e^{-t_2 x' - t_1 y'} \tag{27}$$

where

$$t_1 = i(k_{ym} - k_{yp} \pm k_{zj_{mn}} b)$$
$$t_2 = i(k_{xn} - k_{xo} \pm k_{zj_{mn}} a)$$

and the domain of the integral corresponds to triangles on the grid of Figure 4. A closer examination of Figure 4 reveals that there are four types of triangular domains to be considered, isolated and referred to as triangles u, d, l, and r in Figure 6, each with a unique domain and definition of a, b, and c. Integrals for each of these triangles must be performed separately. In addition, integrals for the special cases of $t_1 = 0, t_2 \neq 0$ and $t_1 \neq 0, t_2 = 0$ must be considered. Results of these integrations are

Triangle u :

$t_1 = 0, t_2 \neq 0$

$$I_{\gamma\delta}^{\pm} = \frac{2\Delta y}{\Delta x} \frac{1}{t_2^2} e^{-t_2 x_\gamma} (1 - e^{-t_2 \Delta x/2})^2 \tag{28}$$

$t_1 \neq 0, t_2 = 0$

$$I_{\gamma\delta}^{\pm} = \frac{\Delta x}{t_1} e^{-t_1 y_\delta} \left(1 - \frac{1}{t_1 \Delta y}(1 - e^{-t_1 \Delta y})\right) \tag{29}$$

$t_1 \neq 0, t_2 \neq 0$

$$I_{\gamma\delta}^{\pm} = \frac{2\Delta y}{\Delta x} \frac{1}{t_2} e^{-t_2(x_\gamma + \frac{\Delta x}{2})} e^{-t_1(y_\delta + \Delta y)} \left\{ \frac{1 - e^{t_5 \Delta x/2}}{t_5} + \frac{1 - e^{-t_4 \Delta x/2}}{t_4} \right\} \tag{30}$$

Triangle d :

$t_1 = 0, t_2 \neq 0$

$$I_{\gamma\delta}^{\pm} = \frac{2\Delta y}{\Delta x} \frac{1}{t_2^2} e^{-t_2 x_\gamma} (1 - e^{-t_2 \Delta x/2})^2 \tag{31}$$

$t_1 \neq 0, t_2 = 0$

$$I_{\gamma\delta}^{\pm} = -\frac{\Delta x}{t_1} e^{-t_1 y_\delta} \left(1 + \frac{1}{t_1 \Delta y}(1 - e^{-t_1 \Delta y})\right) \tag{32}$$

$t_1 \neq 0, t_2 \neq 0$

$$I_{\gamma\delta}^{\pm} = \frac{2\Delta y}{\Delta x} \frac{1}{t_2} e^{-t_2(x_\gamma + \frac{\Delta x}{2})} e^{-t_1(y_\delta - \Delta y)} \left\{ \frac{1 - e^{-t_5 \Delta x/2}}{t_5} + \frac{1 - e^{t_4 \Delta x/2}}{t_4} \right\} \tag{33}$$

Triangle l :

$t_1 = 0, t_2 \neq 0$

$$I_{\gamma\delta}^{\pm} = \frac{2\Delta y}{t_2} \left(1 - \frac{2}{t_2 \Delta x}(1 - e^{-t_2 \Delta x/2})\right) \tag{34}$$

$t_1 \neq 0, t_2 = 0$

$$I_{\gamma\delta}^{\pm} = \frac{\Delta x}{2\Delta y t_1^2} e^{-t_1(y_\delta + \Delta y)} \left(\left(1 - e^{t_1 \Delta y}\right) + e^{2t_1 \Delta y}\left(1 - e^{-t_1 \Delta y}\right) \right) \tag{35}$$

$t_1 \neq 0, t_2 \neq 0$

$$I_{\gamma\delta}^{\pm} = \frac{1}{t_1} e^{-t_1(y_\delta + \Delta y)} \left\{ \frac{1 - e^{t_5 \Delta x/2}}{t_5} - e^{2t_1 \Delta y} \frac{1 - e^{t_4 \Delta x/2}}{t_4} \right\} \tag{36}$$

Triangle r :

$t_1 = 0, t_2 \neq 0$

$$I_{\gamma\delta}^{\pm} = -\frac{2\Delta y}{t_2} e^{-t_2(x_\gamma + \Delta x/2)} \left(1 + \frac{2}{t_2 \Delta x}(1 - e^{t_2 \Delta x/2})\right) \tag{37}$$

$t_1 \neq 0, t_2 = 0$

$$I_{\gamma\delta}^{\pm} = \frac{\Delta x}{2\Delta y t_1^2} e^{-t_1(y_\delta - \Delta y)} \left((1 - e^{-t_1 \Delta y}) + e^{-2t_1 \Delta y}(1 - e^{t_1 \Delta y})\right) \tag{38}$$

$t_1 \neq 0, t_2 \neq 0$

$$I_{\gamma\delta}^{\pm} = \frac{1}{t_1} e^{-t_1(y_\delta + \Delta y)} e^{-t_2(x_\gamma + \Delta x/2)}$$

$$\left\{ e^{2t_1 \Delta y} \frac{1 - e^{-t_5 \Delta x/2}}{t_5} - \frac{1 - e^{-t_4 \Delta x/2}}{t_4} \right\} \tag{39}$$

where

$$t_4 = -t_2 - t_1 2 \frac{\Delta y}{\Delta x}$$

$$t_5 = -t_2 + t_1 2 \frac{\Delta y}{\Delta x}$$

and $x_\gamma, y_\delta, \Delta x$, and Δy are as defined in Figure 4.

Thus, evaluation of the matrix elements for equation (19) requires summing the analytical expressions above for each facet of the surface profile multiplied by the appropriate vector products for each of the eight matrix elements involving this integral. This procedure is repeated for every combination of the $[mn]$ and $[op]$ indices, with the final number of operations proportional to $m \times n \times o \times p \times f \times 2$ where f is the number of facets making up the profile. Since integrals are performed analytically in this formulation, the only numerical approximation used involves truncation of the surface field unknown Fourier series.

A direct LU inversion technique was used for the matrix equation (19), although more efficient methods could potentially be applied. Note that a direct inversion of the matrix equation requires retaining an equal number of $m \times n$ scattered modes and $o \times p$ Fourier series coefficients. Individual indices m, n, o, and p do not necessarily range over the same values, although a symmetric expansion about zero seems reasonable, especially for a normally incident plane wave field, and was adopted in the results to be presented. Although only direct solutions with square matrices are considered in this paper, use

of non-square matrices inverted with a singular value decomposition technique has been reported for one dimensional periodic surfaces in the literature [10] and has shown potential for avoiding the EBC's conditioning problems.
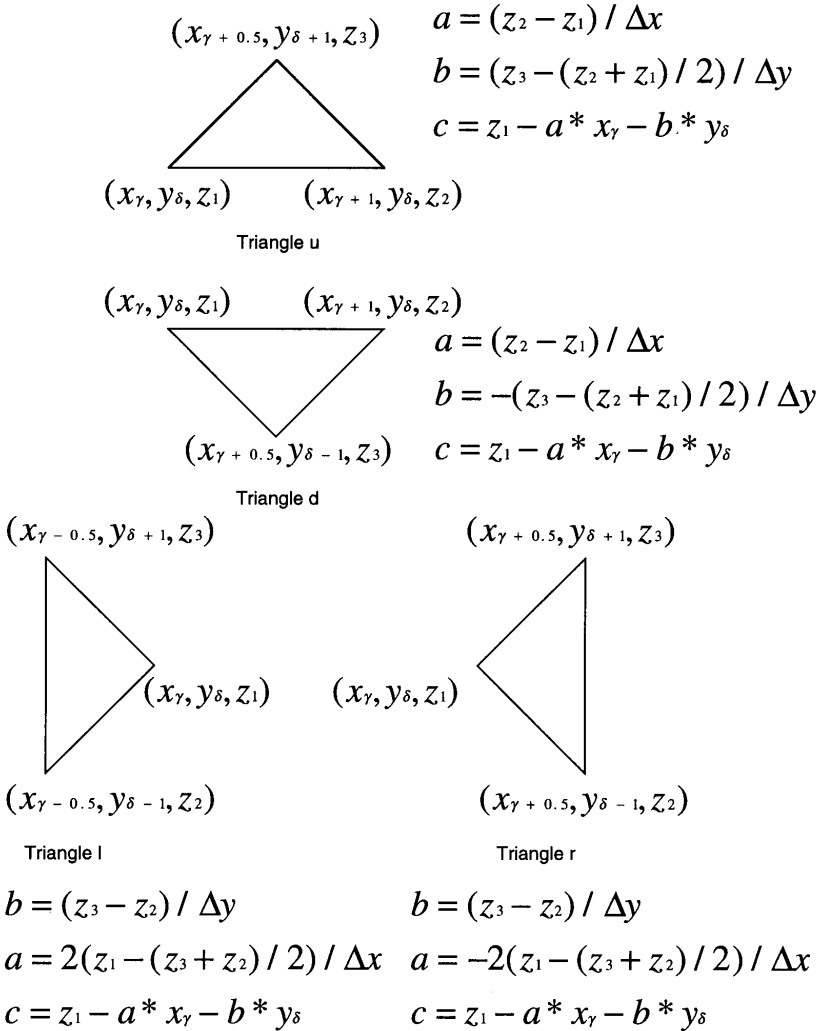
$$(x_{\gamma + 0.5}, y_{\delta + 1}, z_3)$$

$$a = (z_2 - z_1) / \Delta x$$
$$b = (z_3 - (z_2 + z_1) / 2) / \Delta y$$
$$c = z_1 - a * x_\gamma - b * y_\delta$$

$$(x_\gamma, y_\delta, z_1) \qquad (x_{\gamma + 1}, y_\delta, z_2)$$

Triangle u

$$(x_\gamma, y_\delta, z_1) \qquad (x_{\gamma + 1}, y_\delta, z_2)$$

$$a = (z_2 - z_1) / \Delta x$$
$$b = -(z_3 - (z_2 + z_1) / 2) / \Delta y$$

$$(x_{\gamma + 0.5}, y_{\delta - 1}, z_3) \qquad c = z_1 - a * x_\gamma - b * y_\delta$$

Triangle d

$$(x_{\gamma - 0.5}, y_{\delta + 1}, z_3) \qquad\qquad\qquad (x_{\gamma + 0.5}, y_{\delta + 1}, z_3)$$

$$(x_\gamma, y_\delta, z_1) \qquad (x_\gamma, y_\delta, z_1)$$

$$(x_{\gamma - 0.5}, y_{\delta - 1}, z_2) \qquad\qquad\qquad (x_{\gamma + 0.5}, y_{\delta - 1}, z_2)$$

Triangle l   Triangle r

$$b = (z_3 - z_2) / \Delta y \qquad\qquad b = (z_3 - z_2) / \Delta y$$
$$a = 2(z_1 - (z_3 + z_2) / 2) / \Delta x \quad a = -2(z_1 - (z_3 + z_2) / 2) / \Delta x$$
$$c = z_1 - a * x_\gamma - b * y_\delta \qquad c = z_1 - a * x_\gamma - b * y_\delta$$

Figure 6. Types of triangles in surface grid.

4. Model Validation

To validate the code developed, comparisons were made with both EBC [13] and moment method codes [11] for a one dimensional saw-tooth surface profile as shown in Figure 1. The triangular grid of Figure 4, however, is unable to model a one dimensional surface profile due to the presence of triangles l and r along the lines $x = x_1$ and $x = P_x$ respectively. The modified triangular grid shown in Figure 7 is used instead, which now contains four new triangular domains, lu, ld, ru, and rd, for which the $I_{\gamma\delta}^{\pm}$ integrals must be evaluated. Results are

Triangle lu :

$t_1 = 0, t_2 \neq 0$

$$I_{\gamma\delta}^{\pm} = \frac{\Delta y}{t_2} \left(1 - \frac{2}{t_2 \Delta x}(1 - e^{-t_2 \Delta x/2}) \right) \tag{40}$$

$t_1 \neq 0, t_2 = 0$

$$I_{\gamma\delta}^{\pm} = \frac{\Delta x}{2\Delta y t_1^2} e^{-t_1 y_\delta} \left(-(1 - e^{-t_1 \Delta y}) + \Delta y t_1 \right) \tag{41}$$

$t_1 \neq 0, t_2 \neq 0$

$$I_{\gamma\delta}^{\pm} = \frac{1}{t_1} e^{-t_1(y_\delta + \Delta y)} \left\{ \frac{1 - e^{t_5 \Delta x/2}}{t_5} + e^{t_1 \Delta y} \frac{1 - e^{-t_2 \Delta x/2}}{t_2} \right\} \tag{42}$$

Triangle ld :

$t_1 = 0, t_2 \neq 0$

$$I_{\gamma\delta}^{\pm} = \frac{\Delta y}{t_2} \left(1 - \frac{2}{t_2 \Delta x}(1 - e^{-t_2 \Delta x/2}) \right) \tag{43}$$

$t_1 \neq 0, t_2 = 0$

$$I_{\gamma\delta}^{\pm} = - \frac{\Delta x}{2\Delta y t_1^2} e^{-t_1 y_\delta} \left(-e^{t_1 \Delta y}(1 - e^{-t_1 \Delta y}) + \Delta y t_1 \right) \tag{44}$$

$t_1 \neq 0, t_2 \neq 0$

$$I_{\gamma\delta}^{\pm} = \frac{1}{t_1} e^{-t_1(y_\delta + \Delta y)} \left\{ -e^{t_1 \Delta y} \frac{1 - e^{-t_2 \Delta x/2}}{t_2} - e^{2t_1 \Delta y} \frac{1 - e^{t_4 \Delta x/2}}{t_4} \right\} \tag{45}$$

Triangle ru :

$t_1 = 0, t_2 \neq 0$

$$I_{\gamma\delta}^{\pm} = - \frac{\Delta y}{t_2} e^{-t_2(x_\gamma + \Delta x/2)} \left(1 + \frac{2}{t_2 \Delta x}(1 - e^{t_2 \Delta x/2}) \right) \tag{46}$$

$t_1 \neq 0, t_2 = 0$

$$I_{\gamma\delta}^{\pm} = \frac{\Delta x}{2\Delta y t_1^2} e^{-t_1(y_\delta - \Delta y)} \left(\Delta y t_1 e^{-t_1 \Delta y} \right) + e^{-2t_1 \Delta y} (1 - e^{t_1 \Delta y})) \quad (47)$$

$t_1 \neq 0, t_2 \neq 0$

$$I_{\gamma\delta}^{\pm} = \frac{1}{t_1} e^{-t_1 y_\delta} e^{-t_2 x_\gamma} \left\{ \frac{1 - e^{t_4 \Delta x/2}}{t_4} + \frac{1 - e^{-t_2 \Delta x/2}}{t_2} \right\} \quad (48)$$

Triangle rd :

$t_1 = 0, t_2 \neq 0$

$$I_{\gamma\delta}^{\pm} = -\frac{\Delta y}{t_2} e^{-t_2(x_\gamma + \Delta x/2)} \left(1 + \frac{2}{t_2 \Delta x} (1 - e^{t_2 \Delta x/2}) \right) \quad (49)$$

$t_1 \neq 0, t_2 = 0$

$$I_{\gamma\delta}^{\pm} = \frac{\Delta x}{2\Delta y t_1^2} e^{-t_1(y_\delta - \Delta y)} \left(-\Delta y t_1 e^{-t_1 \Delta y} \right) + (1 - e^{-t_1 \Delta y})) \quad (50)$$

$t_1 \neq 0, t_2 \neq 0$

$$I_{\gamma\delta}^{\pm} = \frac{1}{t_1} e^{-t_1 y_\delta} e^{-t_2 x_\gamma} \left\{ \frac{e^{t_5 \Delta x/2} - 1}{t_5} - \frac{1 - e^{-t_2 \Delta x/2}}{t_2} \right\} \quad (51)$$
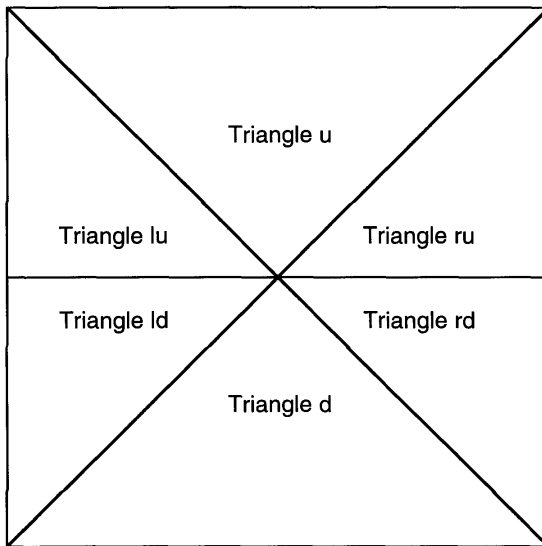

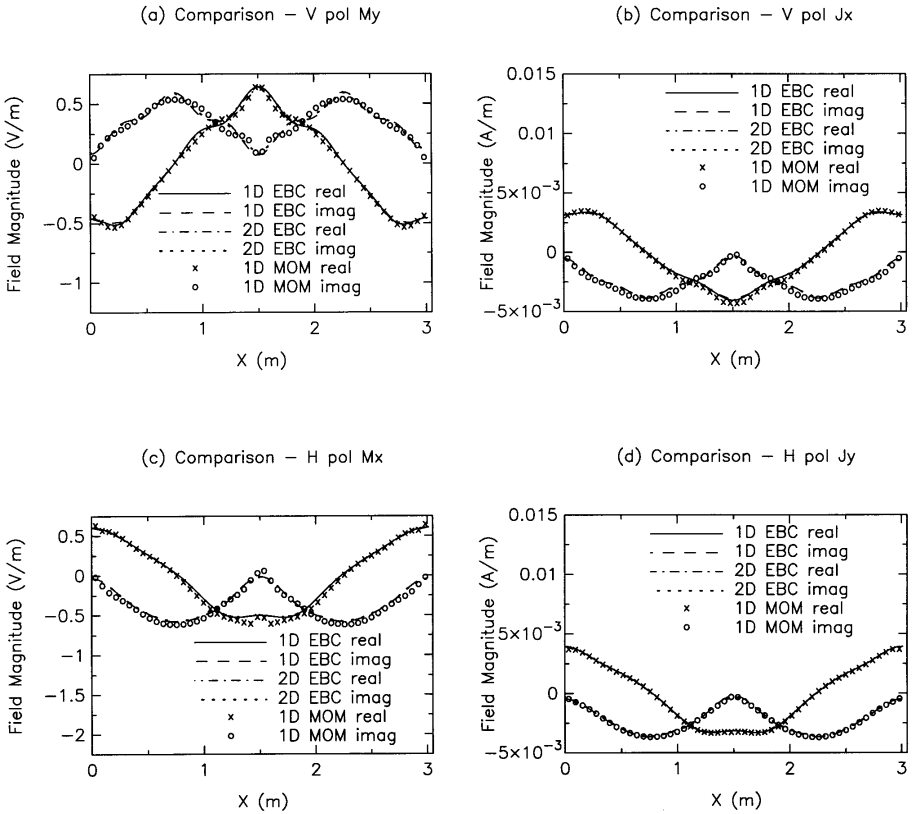Figure 7. Modified triangular grid in $x - y$ plane for 1-D wedge profile.

(a) Comparison − V pol My

(b) Comparison − V pol Jx

(c) Comparison − H pol Mx

(d) Comparison − H pol Jy

Figure 8. Comparison of induced currents on one dimensional wedge profile (a) M_y (b) J_x (c) M_x (d) J_y.

   Construction of a sawtooth profile now requires only two points specified on the surface profile, (x_1, y_1) and $(x_{3/2}, y_2)$ which are set equal to 0 and h, the height of the sawtooth profile, respectively. Calculations were performed for a surface height of 0.5λ, period 3.01λ, dielectric constant $(6, 0)$ and a normally incident plane wave field. Predicted values for the induced currents on the surface profile are plotted in Figure 8 for the one dimensional EBC, one dimensional MOM, and two dimensional EBC codes. A total of 13 Fourier series terms were used with the one dimensional EBC, 169 terms with the two dimensional EBC (using $m = -6$ to 6 and $n = -6$ to 6 as the period in the x direction was set to 3.01λ also), and 50 pulse basis functions in the point matching MOM code, corresponding to 6 points per

wavelength sampling in the dielectric medium. Surface currents M_y and J_x are plotted in Figures 8 (a) and (b) for a vertically polarized incident field, meaning that the unit magnitude incident electric field is directed along the row direction of the surface profile, while surface currents M_x and J_y are plotted in Figure 8 (c) and (d) for a horizontally polarized incident field. Power conservation for all three codes was within 1%, and predicted brightness temperatures as discussed in the next section differed by less than 0.5 K under the assumption of a 300 K surface temperature. These comparisons show that the two dimensional EBC model correctly reduces to the one dimensional surface case, and also that the extended boundary condition approach yields an accurate solution when compared to the method of moments for the sawtooth profile considered. Note that the accuracy of the EBC for this profile is not immediately obvious, as induced surface currents near the edges of the surface have potentially singular behavior. Moment method results were also generated using larger numbers of basis functions and showed that no strong singular behavior occurred near the edges of the wedge profile.

Figure 9 illustrates the convergence of predicted reflectivities with the total number of surface field Fourier coefficients retained for a pyramidal type surface as shown in Figure 3. A surface height of 0.5λ, period in the x and y directions of 3 and 6 λ respectively and a dielectric constant of $(6, 0)$ is used, and total reflected powers are plotted in Figures 9 (a) and (b) for a normally incident plane wave in horizontal and vertical polarizations respectively. The resulting power conservation corresponding to Figures 9 (a) and (b) is also plotted in Figures 9 (c) and (d), and illustrates a clear convergence as the number of surface field mode amplitudes approaches and exceeds 121. Convergence of the predicted total reflected power is of primary concern since this quantity determines the brightness temperature as described in the next section. The results of Figure 9 indicate the accuracy of the EBC approach for the relatively smooth pyramidal surfaces to be considered in this paper, and show that 169 surface field Fourier coefficients should be sufficient to model induced current variations. The remaining calculations of this paper were generated using 169 coefficients, which results in a matrix size of 676 by 676, and required approximately 70 seconds of CPU time on a DEC AXP 3000-M800 for each brightness temperature point.

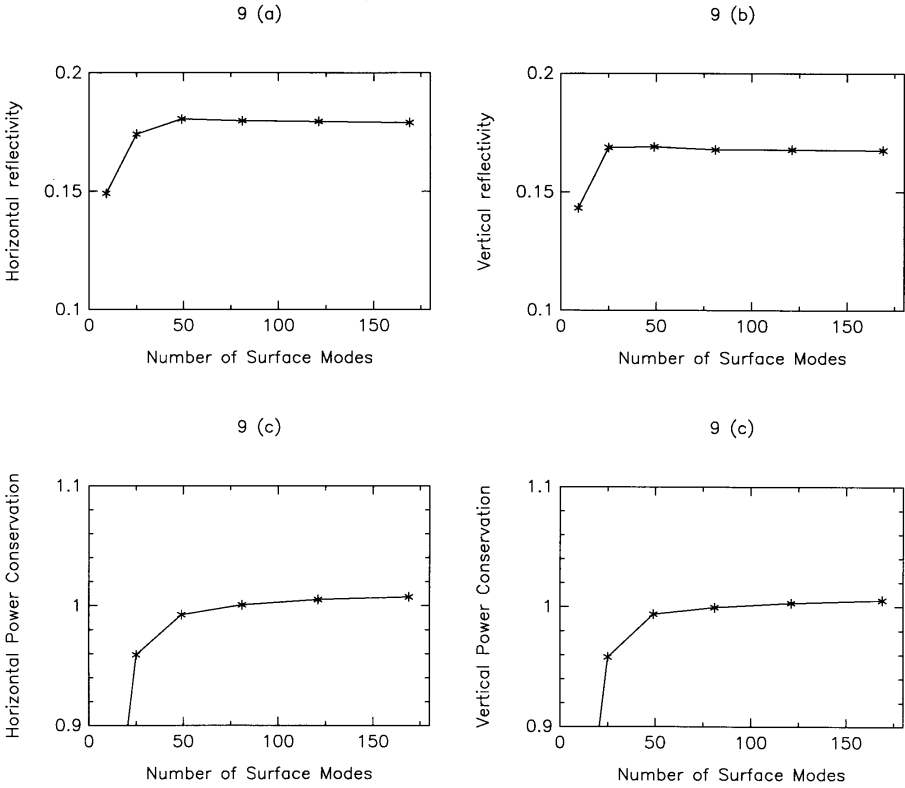9 (a)   9 (b)

Figure 9. Convergence of total reflected power with number of Fourier coefficients (a) Horizontal incidence (b) Vertical incidence (c) Horizontal power conservation (d) Vertical power conservation.

5. Pyramidal Surface Thermal Emission

To assess the response of the third Stokes brightness temperature to degree of surface azimuthal anisotropy, the two dimensionally periodic surface scattering model developed is applied in a study of polarimetric thermal emission from pyramidal surfaces, as shown in Figure 3, for which the faceted surface model approach should be very efficient. The pyramidal surfaces studied are made up of only 4 triangular facets, corresponding to including only the points (x_1, y_1)

and $(x_{3/2}, y_2)$ in the surface profile description, with remaining surface facets generated by the required periodicities.

In polarimetric passive remote sensing, brightness temperatures corresponding to all four modified Stokes parameters are investigated in polarimetric passive remote sensing. The brightness temperature Stokes vector is defined as

$$
\bar{T}_B = \frac{1}{C}\bar{I} = \frac{1}{C}\begin{bmatrix} I_h \\ I_v \\ U \\ V \end{bmatrix} = \frac{1}{\eta C}\begin{bmatrix} \langle E_h E_h^* \rangle \\ \langle E_v E_v^* \rangle \\ 2\mathrm{Re}\langle E_v E_h^* \rangle \\ 2\mathrm{Im}\langle E_v E_h^* \rangle \end{bmatrix} \tag{52}
$$

In the above equation, E_h and E_v are the horizontally and vertically polarized emitted electric fields, η is the characteristic impedance of free space, and $C = k/\lambda^2$ with K denoting Boltzmann's constant, λ the wavelength. The first two parameters of the brightness temperature Stokes vector correspond to the received powers for horizontal and vertical polarizations, respectively. The third and fourth parameters correspond to the complex correlation between electric fields received in horizontal and vertical polarizations. These four parameters are labeled T_{Bh}, T_{Bv}, U_B, and V_B, respectively in this paper.

It is shown in [11] that the third and fourth Stokes parameters may be related to the brightness temperatures in a 45 degree linearly polarized measurement (T_{Bp}) and a right-hand circularly polarized measurement (T_{Br}) as follows:

$$
U_B = 2T_{Bp} - T_{Bh} - T_{Bv} \tag{53}
$$

$$
V_B = 2T_{Br} - T_{Bh} - T_{Bv} \tag{54}
$$

Thus, to compute all four parameters of the Stokes vector, brightness temperatures in horizontal, vertical, 45 linear, and right-hand circular polarizations are first calculated, and the above equations are used to obtain U_B and V_B.

The emissivity of an object is defined as the ratio of the brightness temperature emitted by the object to its actual physical temperature, under the assumption that the object is at a constant physical temperature T_{phys},

$$
T_{Ba} = e_a(\theta, \phi)T_{phys} \tag{55}
$$

In the above equation, the subscript a refers to the polarization of the brightness temperature, θ to the polar observation angle, and ϕ

to the azimuthal observation angle. Through the principles of energy conservation and reciprocity, Kirchhoff's Law relates this emissivity to the reflectivity of the surface [25]:

$$e_a(\theta, \phi) = 1 - r_a(\theta, \phi) \tag{56}$$

The reflectivity $r_a(\theta, \phi)$ for the given incident polarization a is defined as the fraction of the power incident from direction (θ, ϕ) that is rescattered, and is evaluated through calculation of the scattering mode amplitudes $\overline{a}_{mn}$ for the specified pyramidal surface. Due to the periodic nature of the surface profile, the net power reflected from the surface travels only in the $\hat{z}$ direction, so that the total reflectivity of the surface can be written as

$$r_a(\theta, \phi) = \sum_m \sum_n \frac{Re\{k_{z0_{mn}}\}}{|k_{zi}|} |\overline{a}_{mn}|^2 \tag{57}$$

Thus, to determine polarimetric thermal emission from a pyramidal surface, reflected mode amplitudes $\overline{a}_{mn}$ are calculated for an incident field polarized in each of four directions. Note that this requires only one matrix generation and inversion procedure since only the right hand side of the matrix equation varies with different incident fields. Reflectivities, emissivities, and polarimetric brightness temperatures are then calculated from these modes as described previously. A physical temperature of 300 K is assumed for all of the surfaces studied in this section.

The total power transmitted into the surface medium can also be calculated similarly from the $\overline{c}_{mn}$ amplitudes, and a power conservation check can be performed to insure code accuracy. Power conservation errors lead to differences in brightness temperatures computed with $1 - r_a(\theta, \phi)$ from those computed using $e_a(\theta, \phi)$ which is obtained from the power absorbed in the medium. For the results presented in this section, the maximum power conservation error was 0.7% with a corresponding maximum uncertainty in T_{Bh} and T_{Bv} brightness temperatures of 2 K. Brightnesses calculated using the power absorbed exceeded those calculated using one minus the reflectivity in all cases. Azimuthal variations in these brightness temperatures and the corresponding U_B brightnesses, however, were found to have a maximum uncertainty of 0.7 K from the two methods, indicating the insensitivity of the U_B brightness to these errors. Azimuthal variations and U_B

brightnesses were larger using the $1 - r_a(\theta, \phi)$ calculation. Thus, a maximum uncertainty of approximately 2 K in the absolute level of T_{Bh} and T_{Bv} results in this study, with a maximum uncertainty of 0.7 K in T_{Bh} and T_{Bv} azimuth variations and in the U_B brightness temperature. The following results are those calculated using the one minus reflectivity approach.

Figure 10 presents predicted polarimetric brightness temperatures for a pyramidal surface with a height of 0.5λ, period in the x direction of 3.01λ and a varying period in the y direction, ranging from 3.01 to 24.08λ. A period of 3.01λ was chosen to avoid any resonance effects due to the $n = 3, m = 0$ scattered Floquet mode transition from non-propagating to propagating, which would occur for a period of 3λ. A dielectric constant of $(6, 0)$ is assumed for the surface medium. Note that the slopes of this surface are no greater than those for which the wedge profile validation was performed in the previous section, so that the EBC approach should be valid for this surface. Brightness temperatures are plotted for a 0 degree polar observation angle, (nadir looking), and for azimuthal angle, ϕ, varying from 0 (along the $+x$ direction) to 90 degrees (along the $+y$ direction). The expected $\sin 2\phi$ variation of the U_B brightness required for nadir observation due to the reflection symmetries of the surface profile [19] is observed. Also, the $P_y = 3.01\lambda$ curve illustrates the zero value of U_B obtained for nadir observation due to the square pyramid reflection symmetries at 0, 45, and 90 degrees. The response of U_B to the level of anisotropy of the surface is clearly demonstrated in Figure 10, which shows that values of U_B predicted assuming a very large value of P_y significantly overestimate U_B values obtained in the $P_y = 2P_x$ case. However, the convergence of U_B results for $P_y > 4P_x$ illustrates that azimuthal anisotropy beyond this level has little effect.
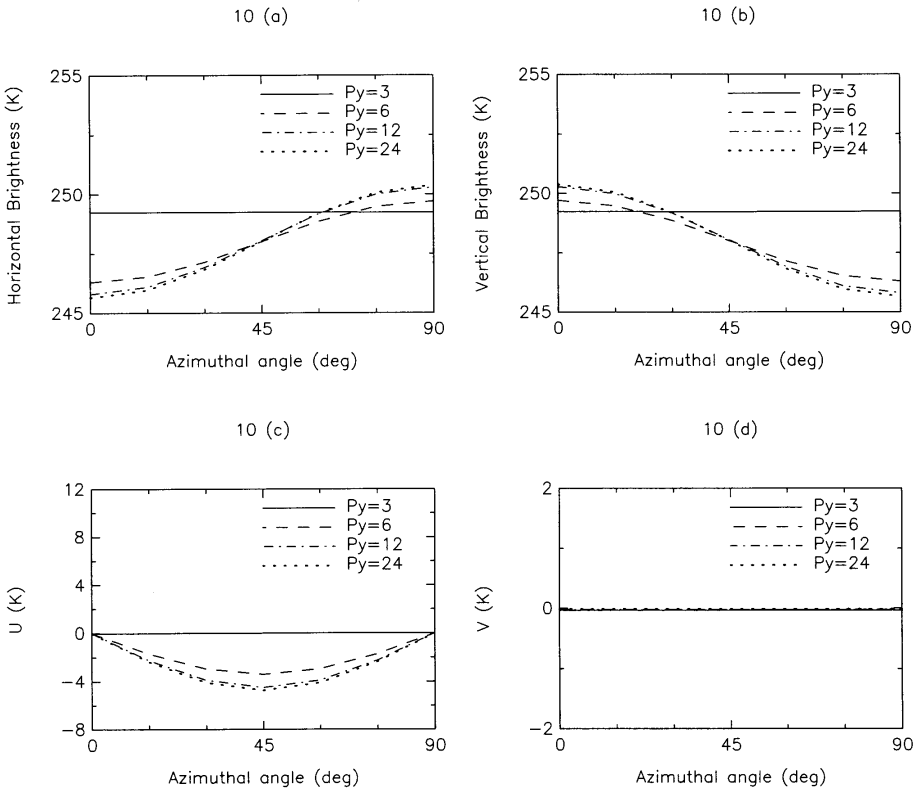
10 (a)

10 (b)

10 (c)

10 (d)

Figure 10. Predicted polarimetric brightness temperatures from a pyramidal surface: Variation with P_y (a) T_{Bh} (b) T_{Bv} (c) U_B (d) V_B

The response of the polarimetric brightness temperatures to pyramidal surface height is plotted in Figure 11, for nadir observation, $P_x = 3.01\lambda$, $P_y = 6.02\lambda$, and a dielectric constant of $(6, 0)$. The response of U_B to surface slope, as indicated by higher U_B values for larger surface heights, is demonstrated in Figure 11. This response has been observed in the literature for 1-D periodic surfaces [11,16]. Surfaces with heights less than 0.25λ and maximum slopes consequently less than 0.08 are seen to produce negligible U_B emission.
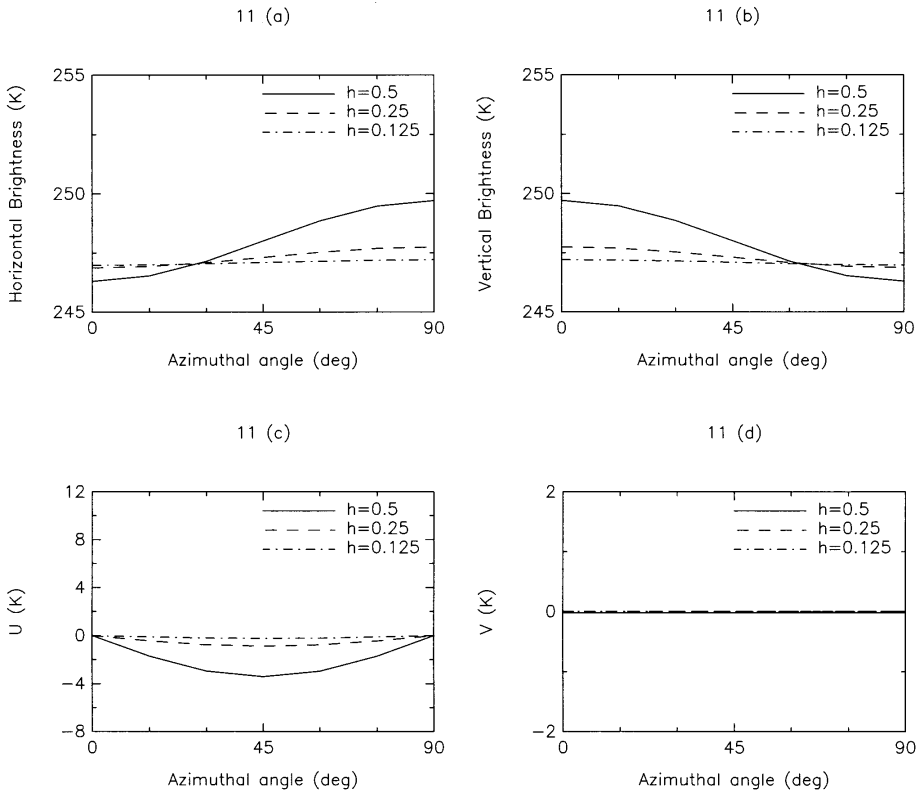
11 (a)

11 (b)

11 (c)

11 (d)

Figure 11. Predicted polarimetric brightness temperatures from a pyramidal surface: Variation with surface height (a) T_{Bh} **(b)** T_{Bv} **(c)** U_B **(d)** V_B

The response of the polarimetric brightness temperatures to polar observation angle is plotted in Figure 12, for pyramidal surfaces with height 0.5λ, $P_x = 3.01\lambda$, $P_y = 6.02\lambda$, and dielectric constant of $(6,0)$. Only variations in the T_{Bh} and T_{Bv} brightness temperatures with azimuthal angle are illustrated in Figures 12 (a) and (b), due to the strong response of the mean T_{Bh} and T_{Bv} brightnesses to polar angle variations for these relatively low dielectric constant materials. Mean values of T_{Bh} and T_{Bv} (averaged over the 7 observation angles computed between 0 and 90 degrees azimuth) are indicated in parentheses in the curve labels of these figures, and the total brightness temperature at a given angle is given by the sum of the deviation

indicated in the figure and the mean value in the curve labels. Responses to polar observation angle similar to those in Figure 12 have been observed for 1-D periodic surfaces [11]. However, simulations in the literature with much higher, ocean like dielectric constant media show smaller variations in U_B with polar observation angle in this range [16]. Also, V_B is observed to show some response to polar observation angle, although it is quite small.
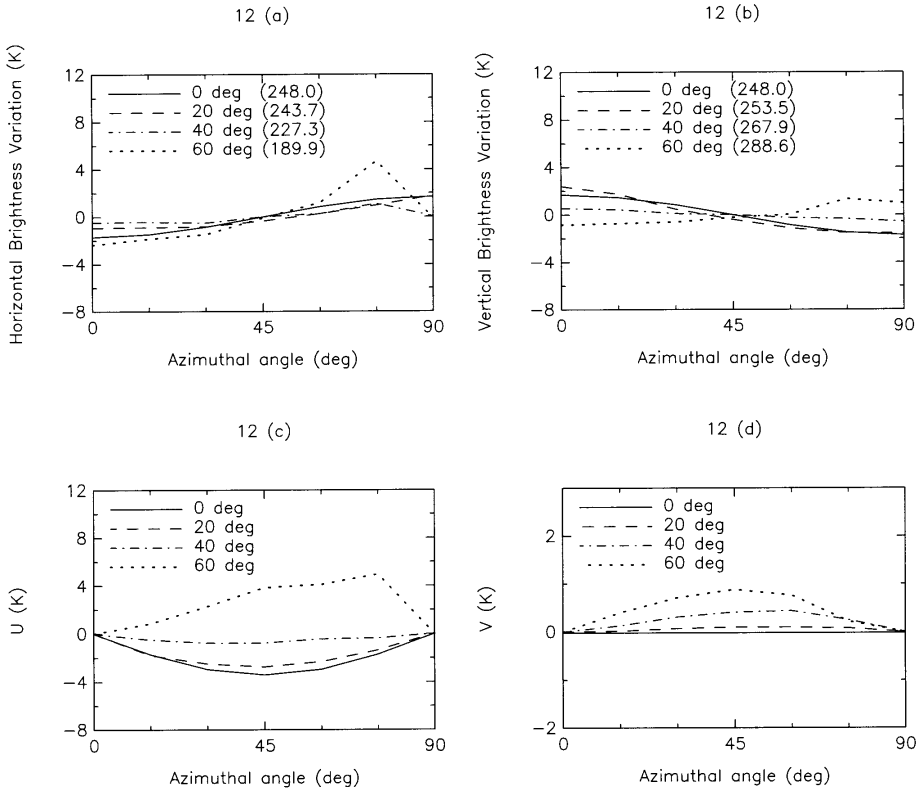

Figure 12. Predicted polarimetric brightness temperatures from a pyramidal surface: Variation with polar angle (a) T_{Bh} azimuth variations (b) T_{Bv} azimuth variations (c) U_B (d) V_B

The response of the polarimetric brightness temperatures to the real part of the surface dielectric constant is plotted in Figure 13, for pyramidal surfaces with height 0.5λ, $P_x = 3.01\lambda$, $P_y = 6.02\lambda$,

and nadir viewing observation. Only azimuth variations in T_{Bh} and T_{Bv} are plotted, again due to the strong influence of dielectric constant variations on mean T_{Bh} and T_{Bv} brightnesses. Note that linear brightness azimuthal variations and the U_B brightness are affected less significantly and still show the same azimuthal signatures. Increasing U_B values obtained are observed to saturate in simulations performed with dielectric constants higher than $(9,0)$.
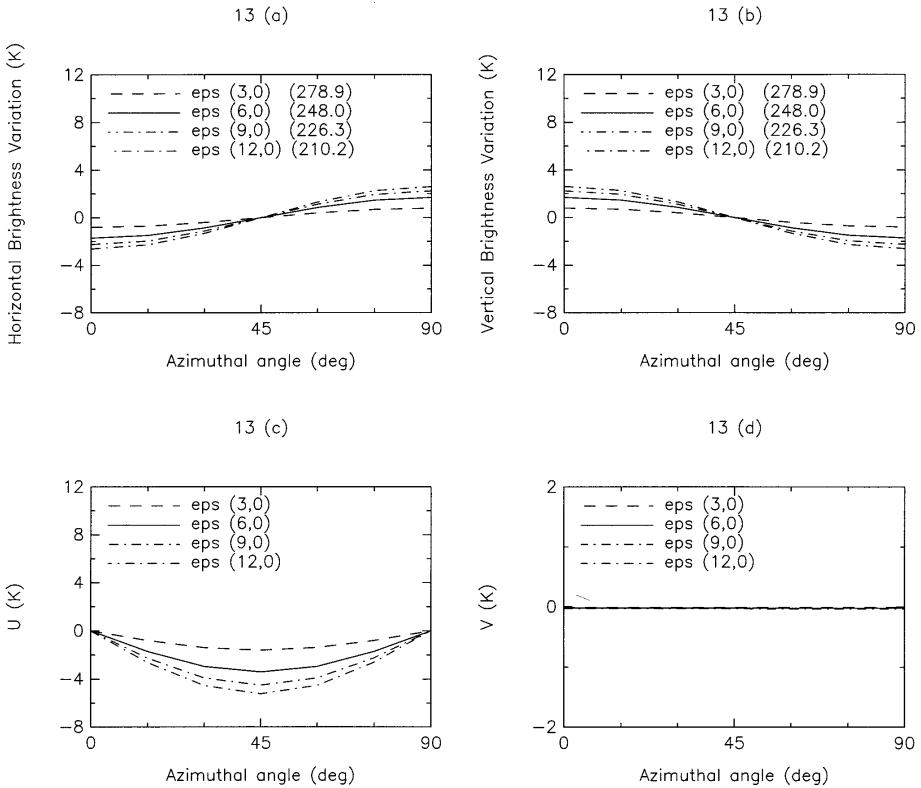

Figure 13. Predicted polarimetric brightness temperatures from a pyramidal surface: Variation with real dielectric constant (a) T_{Bh} azimuth variations (b) T_{Bv} azimuth variations (c) U_B (d) V_B

The response of the polarimetric brightness temperatures to the imaginary part of the surface dielectric constant is plotted in Figure 14, for pyramidal surfaces with height 0.5λ, $P_x = 3.01\lambda$, $P_y = 6.02\lambda$, and nadir viewing observation. Again, the linearly polarized brightness

temperatures show large variations in their means as the imaginary part of the dielectric constant is increased, but azimuth variations and U_B remain relatively unaffected, showing only slight increases with increasing imaginary part.
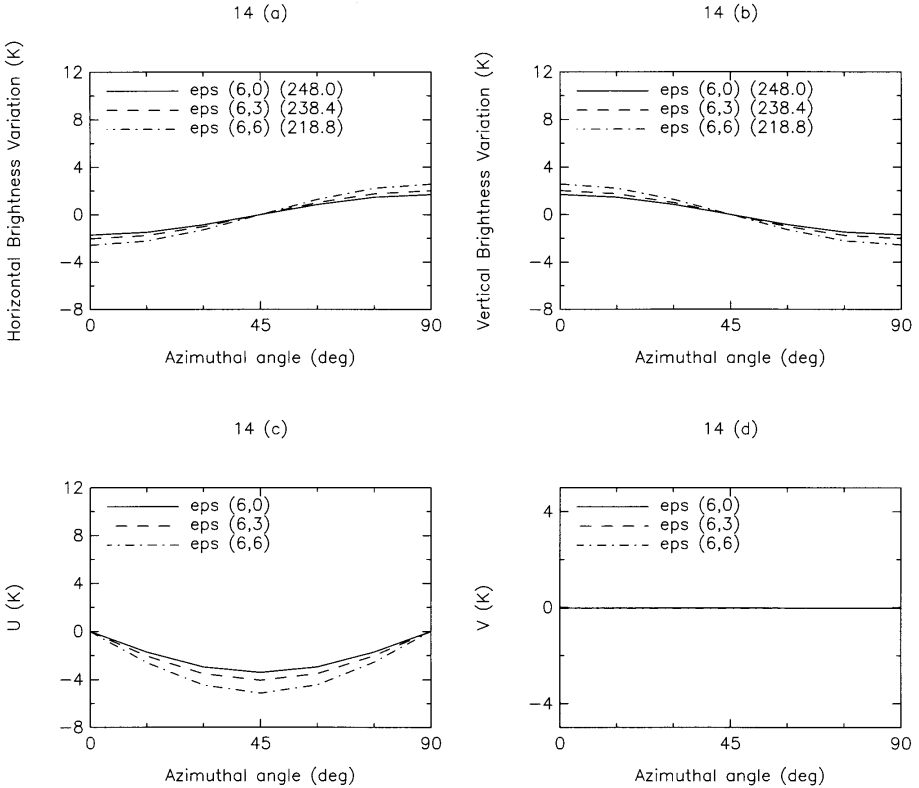

Figure 14. Predicted polarimetric brightness temperatures from a pyramidal surface: Variation with imaginary dielectric constant (a) T_{Bh} azimuth variations (b) T_{Bv} azimuth variations (c) U_B (d) V_B

6. Conclusions

A model for the prediction of scattered Floquet mode amplitudes from a surface periodic in two spatial directions has been developed. This model applies the extended boundary condition approach, and

uses an analytical evaluation of matrix elements over an assumed triangularly faceted surface profile. This method should be very accurate and efficient for surface profiles which are represented in terms of a small number of triangular facets, such as the pyramidal surfaces studied. The model was applied in a study of polarimetric passive remote sensing, and demonstrated that properties of U_B observed in the one dimensional periodic surface case are similar in the two dimensional rough surface case. Also, the response of U_B to the level of anisotropy of the medium under view was studied, and pyramidal surfaces with x to y period ratios greater than 4 were found to show little variation in predicted U_B brightnesses. Other applications of this model include the design of optical gratings and simulation of scattering from two dimensional surfaces at low grazing angles, where the large surface sizes involved in a periodic surface simulation are required.

Acknowledgments

References

1. Rice, S. O., "Reflection of electromagnetic waves from slightly rough surfaces," *Commun. Pure Appl. Math,* Vol. 4, 361–378, 1951.
2. Beckmann, P., and A. Spizzichino, *The Scattering of Electromagnetic Waves from Rough Surfaces,* Pergamon Press, New York, 1963.
3. Chuang, S. L., and J. A. Kong, "Scattering of waves from periodic surfaces," *Proc. of the IEEE,* Vol. 69, 1132–1144, 1981.
4. Zaki, K. A., and A. R. Neureuther, "Scattering from a perfectly conducting surface with a sinusoidal height profile: TE Polarization," *IEEE Trans. Ant. Prop.,* Vol. AP-19, 208–214, 1971.
5. Waterman, P. C., "Scattering by periodic surfaces," *J. Acoust. Soc. Am.,* Vol. 57, 791–802, 1975.
6. Maystre, D., "A new general integral theory for dielectric coated gratings," *J. Opt. Soc. Am.,* Vol. 68, 490–495, 1978.
7. Chuang, S. L., and J. A. Kong, "Wave scattering from a periodic dielectric surface for a general angle of incidence," *Radio Science,* Vol. 17, 545–557, 1982.
8. Moharam, M. G., and T. K. Gaylord, "Diffraction analysis of dielectric surface-relief gratings," *J. Opt. Soc. Am.,* Vol. 72, 1385–

1392, 1982.

9. Kong, J. A., S. L. Lin, and S. L. Chuang, "Microwave Thermal Emission from Periodic Surfaces," *IEEE Trans. Geosc. Electr.,* Vol. GE-22, 377–382, 1984.

10. Barrick, D. E., "Near-grazing illumination and shadowing of rough surfaces," *Radio Science,* Vol. 30, 563–580, 1995.

11. Veysoglu, M. E., H. A. Yueh, R. T. Shin, and J. A. Kong, "Polarimetric passive remote sensing of periodic surfaces," *J. Electromag. Waves Applic.,* Vol. 5, 267–280, 1991.

12. Nghiem, S. V., M. E. Veysoglu, J. A. Kong, R. T. Shin, K. O'Neill, and A. W. Lohanick, "Polarimetric passive remote sensing of a periodic soil surface: microwave measurements and analysis," *J. Electromag. Waves Applic.,* Vol. 5, 997–1005, 1991.

13. Johnson, J. T., J. A. Kong, R. T. Shin, D. H. Staelin, K. O'Neill, and A. Lohanick, "Third Stokes Parameter Emission from a Periodic Water Surface," *IEEE Trans. Geosc. Remote Sens.,* Vol. 31, 1066–1080, 1993.

14. Yueh, S. H., S. V. Nghiem, W. Wilson, F. K. Li, J. T. Johnson, and J. A. Kong, "Polarimetric Passive Remote Sensing of Periodic Water Surfaces," *Radio Science,* Vol. 29, 87–96, 1994.

15. Gasiewski, A. J., and D. B. Kunkee, "Polarized Microwave Emission from Water Waves," *Radio Science,* Vol. 29, 1449–1465, 1994.

16. Johnson, J. T., J. A. Kong, R. T. Shin, S. H. Yueh, S. V. Nghiem, and R. Kwok, "Polarimetric Thermal Emission from Rough Ocean Surfaces," *J. Electromag. Waves Applic.,* Vol. 8, 43–59, 1994.

17. Tsang, L., "Polarimetric passive microwave remote sensing of random discrete scatterers and rough surfaces," *J. of Electromag. Waves Applic.,* Vol. 5, 41–57, 1991.

18. Dzura, M. S., V. S. Etkin, A. S. Khrupin, M. N. Pospelov, and M. D. Raev, "Radiometers Polarimeters: Principles of Design and Applications for Sea Surface Microwave Emission Polarimetry," *IGARSS 92,* conference proceedings, 1432–1434, 1992.

19. Yueh, S. H., R. Kwok, F. K. Li, S. V. Nghiem, and W. J. Wilson, "Polarimetric passive remote sensing of ocean wind vectors," *Radio Science,* Vol. 29, 799–814, 1994.

20. Yueh, S. H., S. V. Nghiem, and R. Kwok, "Comparison of a polarimetric scattering and emission model with ocean backscatter and brightness measurements," *IGARSS 94,* conference proceedings, 1994.

21. Yueh, S. H., W. J. Wilson, F. K. Li, S. V. Nghiem, and W. B. Rick-etts, "Polarimetric Measurements of Sea Surface Brightness Temperatures Using an Aircraft K-Band Radiometer," *IEEE Trans. Geosc. Remote Sens.,* Vol. 33, 85–92, 1995.

22. Yang, C. F., W. D. Burnside, and R. C. Ruddock, "A doubly periodic moment method solution for the analysis and design of an absorber covered wall," *IEEE Trans. Ant. and Prop.,* Vol. 41, 600–609, 1993.

23. Garcia, N., V. Celli, N. Hill, and N. Cabrera, "Ill conditioned matrices in the scattering of waves from hard corrugated surfaces," *Phys. Rev. B,* Vol. 18, 5184–5189, 1978.

24. Wang, J. J. H., *Generalized Moment Methods in Electromagnetics,* Wiley, New York, 1991.

25. Tsang, L., J. A. Kong, and R. T. Shin, *Theory of Microwave Remote Sensing,* Wiley, New York, 1985.